Journal of Materials Chemistry A

ROYAL SOCIETY OF CHEMISTRY

PAPER

View Article Online
View Journal | View Issue

Cite this: J. Mater. Chem. A, 2024, 12, 3722

The grain morphology and surface properties of a Li-rich Li_2MnO_3 cathode material: a first-principles study†

Xiaotong Yan, Xingyu Zhou, Chunwei Zhu, Weijie Huang and Yu-Jun Zhao *

Received 1st November 2023
Accepted 15th December 2023

DOI: 10.1039/d3ta06692d

rsc.li/materials-a

Complex surface evolution plays a critical role in the rapid energy degradation of Li_2MnO_3 as a cathode material for high-energy-density Li-ion batteries. Here, we demonstrate that the defect-containing (001) surface of Li_2MnO_3 satisfies the stoichiometric relationship under air conditions and in the main experimental temperature window. For Li_2MnO_3 cathode materials, the surface area fraction of the terminals that satisfy stoichiometry (STO) can reach at least 70% when the synthesis environments are under Li&Mn-mid and Mn-rich conditions, while it is hard to exceed 40% under Li-rich conditions. All the stable surfaces exhibit excellent electrochemical properties, save the poor charge voltage and conductivity of the (001)_STO terminal. The low p-band center of O ions and stronger Mn–O bond strength effectively prevent the release of oxygen during Li-ion extraction in Li_2MnO_3. In addition, the low surface energy of the (001)_STO terminal and the high energy barrier between the different terminals dominates the dish-shape appearance of the grain morphology.

1 Introduction

In recent years, energy storage has become increasingly important to the world economy,[1] largely due to its critical role in satisfying energy demand and achieving dependence on renewable energy. As a key component of energy storage, research on the performance and characteristics of Li-ion cathode materials has attracted a flurry of attention from academia and industry.[2–5]

Due to its high voltage (as high as 4.5 V),[6] high specific capacity (theoretical capacity of up to 458 mA h g^{-1}), and low cost, Li_2MnO_3 is an attractive alternative to traditional lithium-ion battery cathode materials. It also faces some challenges, though Li_2MnO_3 has many advantageous characteristics and application prospects. For example, its structural stability, cycle life, and capacity degradation issues still need to be much improved.[7–10] Therefore, further research and improvement are crucial for fully exploring the potential of Li_2MnO_3 and its applications in different fields.

Earlier research has demonstrated that the evolution of surface oxygen during the charging process is key for the rapid performance degradation.[6,11–15] To solve this issue, density functional theory (DFT) (on its own or combined with experiments) has been employed to improve the performance of Li-ion cathode materials.[15–20] Qiu *et al.*[21] suppressed the rapid decay in the capacity of Li-rich cathode materials by forming an oxygen vacancy layer approximately 20 nm thick on the surface. Ning *et al.*[22] carried out theoretical and experimental studies on a coating of graphene on the (010) surface of Li_2MnO_3. They demonstrated that the coating of graphene and its defect structure can improve the cycle stability of Li_2MnO_3. Shin *et al.*[23] used high-throughput calculations to screen effective doping elements that inhibit oxygen gas evolution and verified them through experiments. Additionally, Shin *et al.*[24] conducted a theoretical study on the reconstruction of the low Miller index surface of Li_2MnO_3 and the stability of oxygen evolution during the charging process. Wang *et al.*[25] studied the Wulff shape of the low Miller index surface of Li_2MnO_3 at different Li or Mn concentrations. However, the grain morphology stability and properties of Li_2MnO_3 in air have not been well studied, neither experimentally nor theoretically.[9,17,26–28]

In this study, a bond energy model is employed to effectively screen stable Li_2MnO_3 surfaces with Miller indices less than 5, and a crystal morphology similar to the experimental observation is obtained. Then, the transformation mechanisms of stable Li_2MnO_3 surfaces at different temperatures and Li (or Mn) concentrations are systematically investigated. We find that the defect-containing (001) surface of Li_2MnO_3 satisfies the stoichiometric relationship in the main experimental temperature window for the synthesis of Li_2MnO_3. Finally, the electrochemical performance and oxygen evolution characteristics for the stable surfaces are analyzed and compared. It turns out that the low p-band center of the O ion and the stronger Mn–O bond strength effectively prevent the release of oxygen during Li-ion extraction in Li_2MnO_3.

Department of Physics, South China University of Technology, Guangzhou 510640, PR China. E-mail: zhaoyj@scut.edu.cn

† Electronic supplementary information (ESI) available. See DOI: https://doi.org/10.1039/d3ta06692d

2 Computational details

2.1 Computational method

All calculations are performed using the projector augmented wave (PAW) scheme,[29] as implemented in the Vienna *Ab initio* Simulation Package (VASP).[30,31] The exchange–correlation energies are approximated in the generalized gradient approximation (GGA) of Perdew, Burke and Ernzerhof (PBE).[32] The cutoff energy for the plane wave expansion is chosen to be 500 eV. The Γ-centered k-point Brillouin zone sampling is used in the slab calculations, and $5 \times 5 \times 1$ sampling is also included in the convergence test. The lattice parameters and ionic positions are relaxed until the forces on each ion converge to less than 0.01 eV Å^{-1}. Spin polarization is considered in all calculations. In addition, to address on-site Coulomb interactions for the localized 3d electrons of transition metals, additional Hubbard parameter correction is carried out following ref. 33 and 34. Within the GGA+U scheme, a single effective parameter $U_{\text{eff}} = U - J$ is used, and the U_{eff} of 4.5 eV for Mn is determined by a series of tests. Finally, the phonon frequencies are calculated using PHONOPY.[35,36]

2.2 Surface energy calculations

Generally, the most stable surface compositions and geometries at different temperatures (T) and pressures (P) are defined by the surface Gibbs free energy $G^{\text{Surf}}(T, P)$:[37–39]

$$G^{\text{Surf}}(T,P) = \frac{1}{2A}\left[G^{\text{Slab}}(T,P) - G^{\text{Bulk}}(T,P) - \sum_i \Delta n_i \mu_i(T,P)\right], \quad (1)$$

where A is the surface area, and $G^{\text{Slab}}(T,P)$ and $G^{\text{Bulk}}(T,P)$ represent the Gibbs free energies of the slab model and reference bulk structure, respectively. Additionally, i represents any element, and Δn_i is the difference number between the slab model and reference bulk structure for each element i. $\mu_i(T,P)$ is the chemical potential for element i and is defined as follows:

$$\mu_i(T,P) = \Delta\mu_i(T,P) + \mu_i^{\text{Bulk}}(T,P) \quad (2)$$

Here $\mu_i^{\text{Bulk}}(T,P)$ represents the Li, Mn, and O substances, and $\Delta\mu_i(T,P)$ should be no more than 0 to avoid formation of elemental crystal i. In this study, the chemical potential of oxygen, $\mu_{\text{O}}(T,P)$, is delimited as the ideal gas expression:

$$\mu_{\text{O}}(T,P) = \mu_{\text{O}}(T,P_0) + \frac{1}{2}RT\ln\left(\frac{P}{P_0}\right), \quad (3)$$

where $P = 0.21$ atm is the partial pressure of oxygen, $P_0 = 1$ atm represents the standard atmospheric pressure, and R is the ideal gas constant. $\mu_{\text{O}}(T,P_0)$ is the chemical potential of pure oxygen under standard pressure, expressed as below:

$$\begin{aligned}\mu_{\text{O}}(T,P_0) &= \mu_{\text{O}}(0\text{ K},P_0) + \frac{1}{2}\Delta G_{\text{O}_2}(\Delta T,P_0)\\ &= \mu_{\text{O}}(0\text{ K},P_0) + \frac{1}{2}\Delta[H(T,P_0) - TS(T,P_0)]\end{aligned} \quad (4)$$

For $\mu_{\text{O}}(0\text{ K},P_0)$, it corresponds to the free energy of an isolated oxygen molecule at 0 K.[37] $\Delta[H(T,P_0) - TS(T,P_0)]$ can be obtained from NIST/JANAF tables (the chemical potentials of oxygen, $\mu_{\text{O}}(T,P)$, under air are shown in Section S2 of the ESI†).[40] Here, the Gibbs free energy of the solid can be approximated to the Helmholtz free energy, as the contribution of PV can be neglected. The free energy and chemical potential of the solid structure can be expressed as follows:

$$G_i^{\text{Solid}}(T,P) = F_i^{\text{Solid}}(T) + PV \approx F_i^{\text{Solid}}(T) \quad (5)$$

$$\mu_i^{\text{Solid}}(T,P) = \frac{\partial G_i^{\text{Solid}}(T,P)}{\partial n_i} \approx \frac{\partial F_i^{\text{Solid}}(T)}{\partial n_i} \quad (6)$$

In this work, the temperature-dependent part of the Helmholtz free energy considers only the energy contribution of the vibrational terms of the atoms in the corresponding material. The Helmholtz free energy of the bulk structure is defined as follows:

$$F^{\text{Bulk}}(T) = E_{\text{ele}}^{\text{Bulk}} + F_{\text{vib}}^{\text{Bulk}}(T) \quad (7)$$

$$F_{\text{vib}}^{\text{Bulk}}(T) = \sum_{n=1}^{N}\left\{\frac{1}{2}\int_0^{\omega_n^{\max}} g_n(\omega)\hbar\omega_n \mathrm{d}\omega + k_{\text{B}}T\int_0^{\omega_n^{\max}} \ln\left[1 - \exp\left(-\frac{\hbar\omega_n}{k_{\text{B}}T}\right)\right] g_n(\omega)\mathrm{d}\omega\right\} \quad (8)$$

$E_{\text{ele}}^{\text{Bulk}}$ is the electron energy of the bulk structure obtained *via* DFT calculations at 0 K. $F_{\text{vib}}^{\text{Bulk}}(T)$ is the vibrational energy of the atoms in the relevant material, expressed as below:

$$\int_0^{\omega_n^{\max}} g_n(\omega)\mathrm{d}\omega = 3 \quad (9)$$

Here, N is the total number of atoms in the system and n is any atom in the system. ω_n and $\omega_n^{\max}$ represent the vibrational frequency and the maximum vibrational frequency of atom n, respectively. Moreover, $g_n(\omega)$ is the phonon density of states of a particular atom n, where k_{B} and $\hbar$ are the Boltzmann constant and the Planck constant.

For the slab model, the vibrational frequency of the atoms in the surface region can be replaced by the vibrational frequency of the atoms corresponding to the material under bulk structural conditions.[39] Furthermore, after testing (as seen in Section S2†) in the slab model, the contribution of any atom to the

vibrational free energy can be replaced by the average vibrational free energy of the same element. Overall, the Gibbs free energy, $G^{\mathrm{Slab}}(T,P)$, of the slab structure also can be replaced by the Helmholtz free energy, $F^{\mathrm{Slab}}(T,P)$:

$$G^{\mathrm{Slab}}(T,P) \approx F^{\mathrm{Slab}}(T,P) = E_{\mathrm{ele}}^{\mathrm{Slab}} + \sum_{i}\sum_{1}^{N_i} \overline{F_{\mathrm{vib}}{}^{i}(T)} \quad (10)$$

Here, $E_{\mathrm{ele}}^{\mathrm{Slab}}$ is the electron energy of the slab structure obtained *via* DFT calculations at 0 K. N_i is the total number of atoms of any element i, and $\overline{F_{\mathrm{vib}}{}^{i}(T)}$ is the average vibrational energy of element i in the slab structure, which is expressed as below:

$$\overline{F_{\mathrm{vib}}{}^{i}(T)} = \left\{ \sum_{n=1}^{N_i} \left\{ \frac{1}{2}\int_0^{\omega_{ni}^{\max}} g_{ni}(\omega)\hbar\omega_{ni}\mathrm{d}\omega + k_{\mathrm{B}}T\int_0^{\omega_{ni}^{\max}} \ln\left[1-\exp\left(-\frac{\hbar\omega_{ni}}{k_{\mathrm{B}}T}\right)\right] g_{ni}(\omega)\mathrm{d}\omega \right\} \right\} \frac{1}{N_i}, \quad (11)$$

where ω_{ni}, $\omega_{ni}^{\max}$, and $g_{ni}(\omega)$ represent the vibrational frequency, maximum vibrational frequency, and particular phonon density of states of any atom n in element i, respectively.

2.3 Surface structure construction

The surface models are constructed *via* implementation in the *pymatgen* framework[41] with relaxed bulk Li_2MnO_3, where the default thresh is set to 0.2 Å along the normal direction of the surface. The Li_2MnO_3 surfaces are built from a symmetric periodic slab with a layer thickness and vacuum space of more than 15 Å and 10 Å in all cases. In this paper, the lattice constants for Li_2MnO_3 with the stable structure are $a = 5.002$ Å, $b = 8.646$ Å, and $c = 5.077$ Å (space group $C2/m$, as seen in Section S1†), as obtained using GGA+U, and are in line with the experimental results.[24,42] Except for the fact that the bottom one-third of the slab structure is fixed as the bulk structure when calculating the charging platform and the formation energy of oxygen evolution (in Section 3.3), the lattice and ionic positions of the slab structure are all relaxed in all other cases.

3 Results and discussion

3.1 Phase stability of Li_2MnO_3

In this study, Li, Mn, and O_2 are considered as reactants for the generation of Li_2O, MnO_2, and Li_2MnO_3 under air. For Li_2MnO_3, to avoid the formation of a competitive phase, the change in element chemical potential, $\Delta\mu_i(T,P)$, is defined as follows:[43,44]

$$2\Delta\mu_{\mathrm{Li}} + \Delta\mu_{\mathrm{Mn}} + 3\Delta\mu_{\mathrm{O}} = \Delta H_{\mathrm{f}}(\mathrm{Li_2MnO_3}) \quad (12)$$

$$2\Delta\mu_{\mathrm{Li}} + \Delta\mu_{\mathrm{O}} \leq \Delta H_{\mathrm{f}}(\mathrm{Li_2O}) \quad (13)$$

$$\Delta\mu_{\mathrm{Mn}} + 2\Delta\mu_{\mathrm{O}} \leq \Delta H_{\mathrm{f}}(\mathrm{MnO_2}) \quad (14)$$

Consequently, the thermodynamic phase diagram of the system under 0 K conditions is shown in Fig. 1, and the thermodynamic phase diagram area ratios of the different phases generated under different temperature conditions are listed in Table 1.

Fig. 1 and Table 1 imply that the preparation of pure Li_2MnO_3 gets easier as the reaction temperature increases. However, the formation of pure Li_2MnO_3 is nevertheless difficult, and easily accompanied by competing phases. Points F, G, and H represent three typical chemical potential conditions, *i.e.*, Li-rich, Li&Mn-mid, and Mn-rich, respectively, as shown in Fig. 1. The surface energies under these three chemical potential conditions are studied as follows.

3.2 Surface stability and Wulff shape of Li_2MnO_3

To provide a more comprehensive analysis of the grain morphology and surface properties of Li_2MnO_3, a combination of a bond energy model and linear regression analysis (as presented in Section S3†) is applied in this study. We linearly fit the surface energy of the system with the number and type of broken bonds based on relevant literature reports.[45–48] In this study, the surface energies of 309 surfaces, with a total of 1100

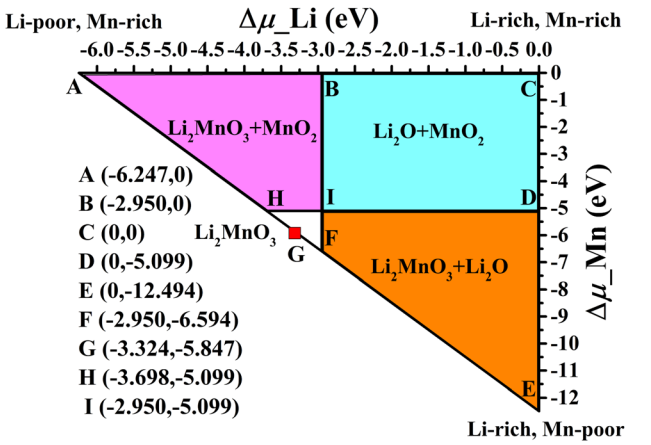

Fig. 1 The thermodynamic phase diagram of Li_2MnO_3 at 0 K.

Table 1 Phase diagram area ratios of different products in the Li–Mn–O system at various temperatures (in %)

Temperature	Li_2O + MnO_2	Li_2MnO_3 + MnO_2	Li_2MnO_3 + Li_2O	Li_2MnO_3
0 K	38.5	26.5	33.6	1.4
300 K	37.5	25.2	35.6	1.7
600 K	35.8	23.8	38.3	2.1
900 K	33.8	22.1	41.5	2.6
1200 K	31.3	20.1	45.4	3.3
1500 K	27.8	17.6	50.4	4.2

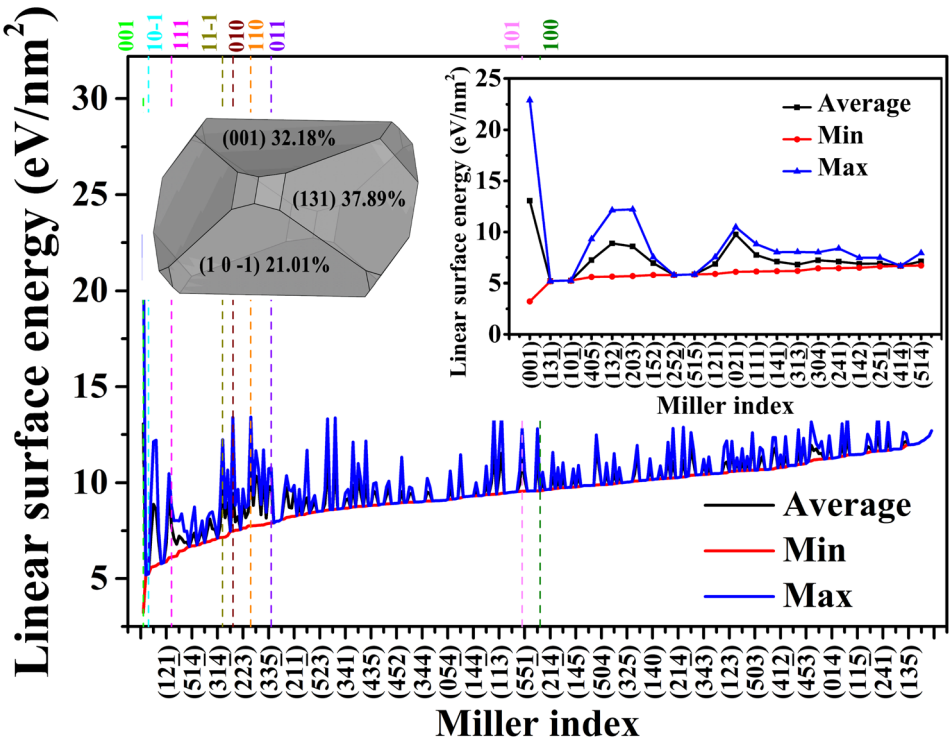

Fig. 2 The surface energies of different surfaces and terminals of Li_2MnO_3 are predicted for Miller indices of less than 5 by linear models.

terminals of Li_2MnO_3, are predicted for Miller indices of less than 5, and the results are shown in Fig. 2. It should be noted that the surfaces with high Miller indices do not easily appear in the crystal morphology because they have high surface energies in general.[49–52] Therefore, we adopt the maximum Miller index value of 5 for the possible surfaces in this study. In fact, surfaces with Miller index values of 3 already do not easily appear according to our calculations (see the Wulff shape in the inset of Fig. 2).

As shown in Fig. 2, the (001) surface is the grain surface with the lowest surface energy, in line with the experimental report that the (001) surface is the dominant surface.[17,26] Meanwhile, the (131) and (10$\bar{1}$) crystal surfaces have the second and third lowest surface energies, respectively. The grain morphology predicted by Wulff theory[53,54] for all surfaces and terminals with Miller indices less than 5 is shown in the inset of Fig. 2, showing a similar result to the experimental single-crystal images (Fig. S4†). The grain morphology mainly consists of three surfaces: (001), (131), and (10$\bar{1}$), which account for 32.18%, 37.89%, and 21.01% (over 90% of the total surface area), respectively. In addition, all surfaces of Li_2MnO_3 with low Miller indices (Miller indices $\leq$1) have relative low surface energies, except for the (101) and (100) surfaces.

It is difficult to develop a good correlation between the grain morphology and the synthesis environment simply based on a traditional bond energy model, which does not take into account the synthesis environment (gas conditions, synthesis temperature, and reactant concentration). Here, the thermodynamic stability of the different terminals on the low Miller index surfaces (including (100), (010), (001), (110), (101), (10$\bar{1}$), (011), (111), and (11$\bar{1}$)) and (131) are investigated based on the surface energy from the bond energy model and the linear regression analysis. Consequently, the grain morphologies of Li_2MnO_3 are obtained at various reaction temperatures and reactant concentrations under air (all terminal structures and their naming convention are described in Section S4†).

The changes in surface energy of Li_2MnO_3 are calculated according to Section 2.2 with different temperatures and different chemical potentials of Li and Mn. The corresponding surface energies are shown in Fig. S11.† It is clear that the (10$\bar{1}$) and (131) surfaces have low surface energies, in line with the above expectations. However, the (001) surface has a high surface energy throughout the typical range of experimental temperatures and with changes in chemical potentials.

Meanwhile, the (001) surface does not appear in the Wulff shape, in contrast to the experimental reports.[9,17,25,26] Actually, the lowest energy surface terminals of the (001) surface are (001)_Li1.5 and (001)_Li0.5Mn1O3 (adjacent surfaces) within the synthesis temperature range, from a Li-rich concentration to Mn-rich concentration (*cf.* Fig. S11†). It is consistent with the bond energy model results, as (001)_Li1.5 and (001)_Li0.5Mn1O3 have the same bond density and bond type. The structures of these two terminals are shown in Fig. 3(a). Therefore, based on the terminal change under different Li (or Mn) conditions, stable terminal structures are established on the (001) surface of Li_2MnO_3 with different Li defect concentrations (the Li defect concentrations of the surfaces are one-third, one-half, and two-thirds, respectively), as shown in Fig. 3(b). Meanwhile, the surface energies of the (001) surface with various terminals (as seen in Fig. S6†), including the Li

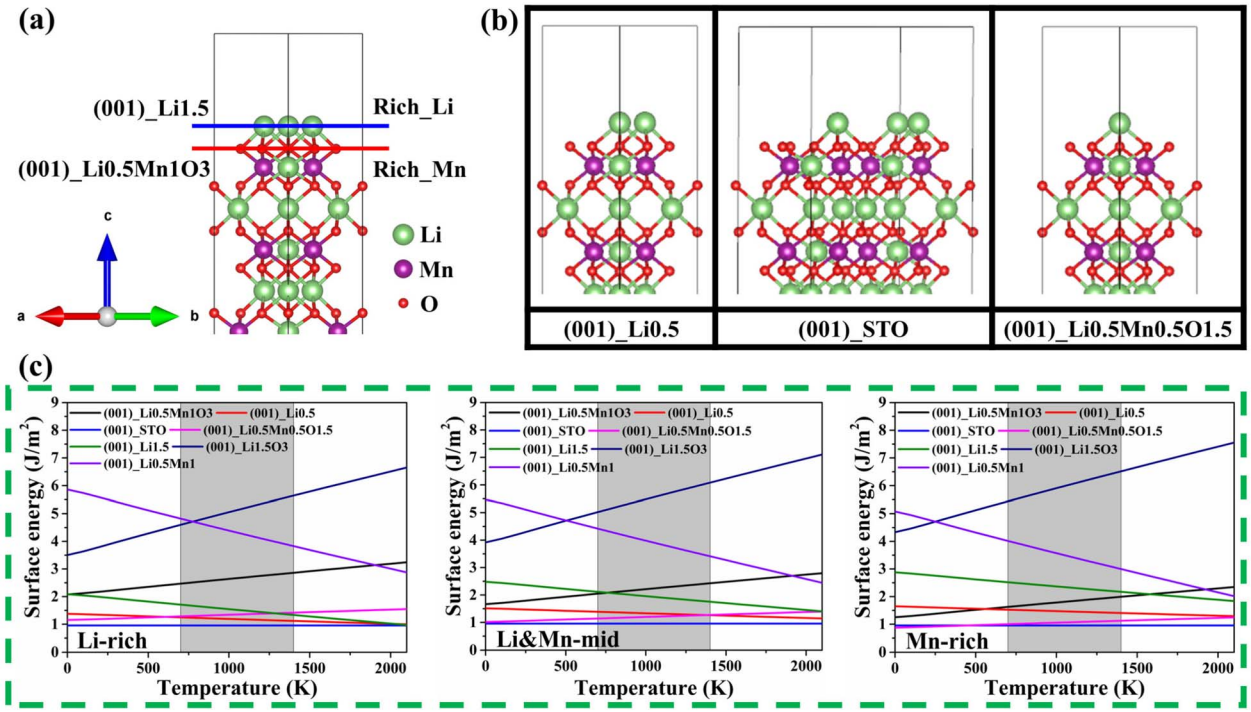

Fig. 3 (a) The changes in the terminal structures of the (001) surface of Li_2MnO_3 in the whole synthesis temperature and chemical potential range. (b) Stable terminal structures of the (001) surface of Li_2MnO_3 with Li-defect concentrations of one-third, one-half, and two-thirds, respectively. (c) The surface energy of the (001) surface of Li_2MnO_3 with different terminals changes with temperature and chemical potential; the gray shading marks the main experimental temperature window for the synthesis of Li_2MnO_3.[24]

defect terminals, are displayed in Fig. 3(c) as a function of the main synthesis temperature at different chemical potentials.

As seen from Fig. 3(c), the Li defect-containing terminals on the (001) surface exhibit low surface energy at the main synthesis temperatures, with the (001)_STO terminal exhibiting the lowest surface energy, *i.e.*, only 0.955 J m^{-2}. The (001)_STO, (10$\bar{1}$)_STO, and (131)_STO terminals have low surface energy largely due to their stoichiometric ratio. We expect that the (100), (11$\bar{1}$), and (110) surfaces (not generated by *pymatgen*) could have low surface energy if they can satisfy the stoichiometric ratio. This could be realized by removing or adding atoms on the terminals. In this study, combined with the above analysis and the results of Section S5,† the stable terminals of the (001) and (100) surfaces are determined to be (001)_STO and (100)_STO. Fig. 4 shows the surface energy changes of the common surfaces with the experimental synthesis temperature and the different chemical potentials of Li or Mn, as well as the Wulff shape of Li_2MnO_3 in the corresponding environments.

As shown in Fig. 4, the stable terminals on the surfaces of (001), (10$\bar{1}$), (131), and (101) under air are (001)_STO, (10$\bar{1}$)_STO, (131)_STO, and (101)_STO, respectively. No terminal transition occurs for these surfaces throughout the synthesis temperature range at three chemical potential definition points. Similarly, the (100)_STO terminal is the main stable (100) surface, whose synthesis temperature is below 1355 K under three typical chemical potential conditions (as shown in Fig. S13†). For the other surfaces, different terminals appear under corresponding chemical potential conditions. As shown in Fig. 4(a), the terminals of (010)_Li1O1, (011)_STO, (11$\bar{1}$)_Li1, (110)_Li1.5O1, and (111)_Li are stable at all synthesis temperatures under the Li-rich chemical potential condition. However, as shown in Fig. 4(b), the terminals of (11$\bar{1}$)_Li1, (110)_Li0.5–2, and (111)_Li1 are stable under the Li&Mn-mid chemical potential condition, while (010) and (011) show a transition to Mn-rich terminals with increasing temperature. As shown in Fig. 4(c), the Mn-rich terminals of (010)_Mn0.5O0.5, (011)_Mn0.5O0.5, (11$\bar{1}$)_Mn0.5O0.5, and (110)_Li0.5Mn1O2 are stable under the Mn-rich chemical potential condition at all synthesis temperatures. Under this chemical potential condition, the surface of (111) changes from the (111)_STO terminal to the (111)_Mn0.5O0.5 terminal with the increase in synthesis temperature.

It is also evident from the analysis of Fig. 4 that the surface energy of Li&O-rich terminals increases as temperature rises. However, the surface energy of the Li-rich and Mn-rich terminals shows an opposite trend with respect to the temperature. In addition, when analyzing the Wulff shapes at different temperatures, shown in Fig. 4, it is interesting that only seven surfaces appear out of the ten studied surfaces. Due to their relatively high surface energy, the surfaces of (100), (101), and (011) are barely visible. Meanwhile, different terminals of the (010) surface appear under Li-rich or Mn-rich chemical potential conditions, and its surface area changes as the temperature increases. The changes in the surface area fraction with temperature under three typical chemical potential conditions, determined by the Wulff theory, are shown in Fig. 5.

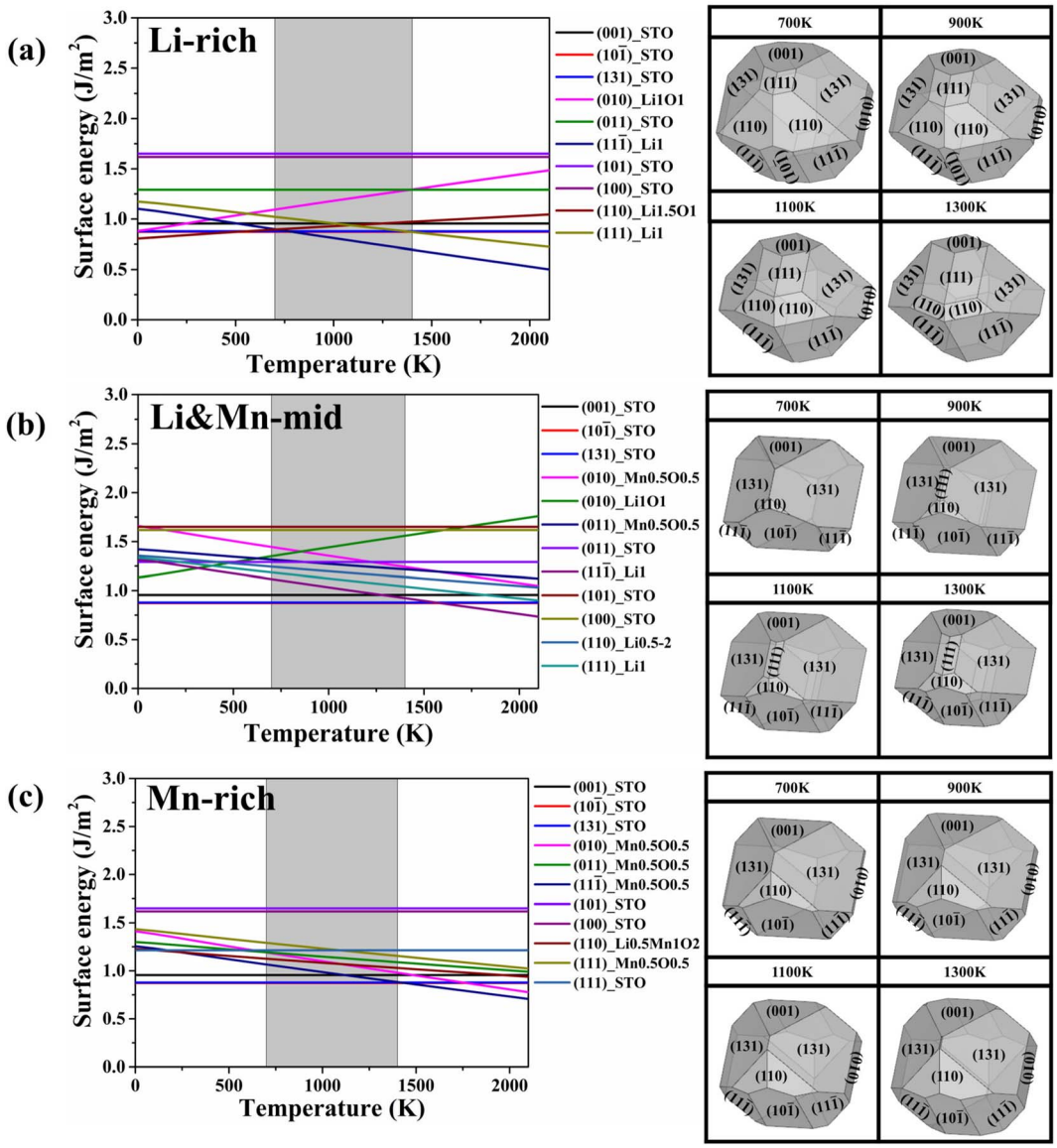

Fig. 4 The surface energy change of the stable surfaces of Li_2MnO_3 at different temperatures and different chemical potentials of Li and Mn ((a) Li-rich, (b) Li&Mn-mid, and (c) Mn-rich), as well as the corresponding Wulff shapes. The regions marked with gray shadows represent the main experimental temperature window for the synthesis of Li_2MnO_3.[24]

From Fig. 5, we notice that the total area fractions of the STO-terminated (131), (10$\bar{1}$), and (001) surfaces show a decreasing trend as the temperature increases. Moreover, the fraction of STO-terminals in the total surface area first increases and then decreases as the synthesis environment of the system transitions from Li-rich to Mn-rich conditions. When the synthesis environments are Li&Mn-mid and Mn-rich, the surface fraction of STO-terminals can reach at least 70%, but it is difficult to exceed 40% under Li-rich conditions. From Fig. 5(a), it can be seen that the (131) and (11$\bar{1}$) surfaces are the main surfaces under Li-rich conditions at all synthesis temperatures. For the (111) and (11$\bar{1}$) surfaces, the area fraction increases with increasing temperature, while a downward trend in area is observed for the other surfaces. In particular, when the temperature exceeds 1000 K, the surfaces of (010) and (10$\bar{1}$) almost disappear. As shown in Fig. 5(b), the surface area fraction of (111), (110), and (11$\bar{1}$) increases with increasing temperature under the Li&Mn-mid condition. The area fraction of the (001) surface remains almost unchanged. It can be seen from Fig. 5(c) that in the case of the Mn-rich state, the surface area fractions of the (11$\bar{1}$) and (010) surfaces increase with increasing temperature. For the (110) and (001) surfaces, their area fraction remains stable with an increase in temperature.

3.3 Properties of the surface and surface influence zone (SIZ) of Li_2MnO_3

From the analysis of the results in Section 3.2, 11 terminals of the seven surfaces exist stably as the surfaces of the Li_2MnO_3 grain. Therefore, the performances of these 11 terminals are

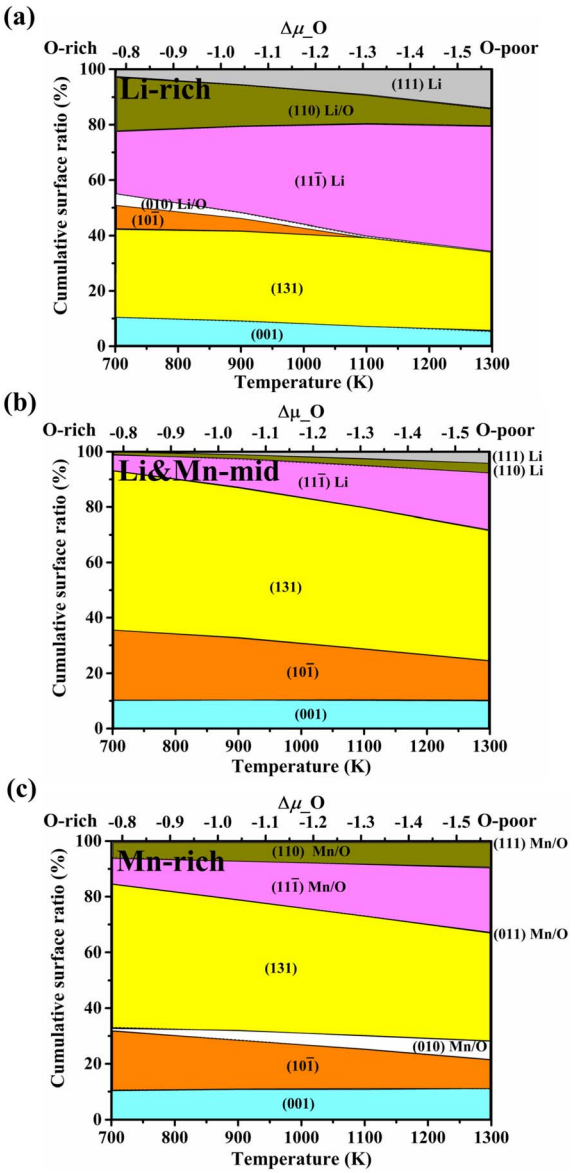

Fig. 5 The percentage of surface area *vs.* the main synthesis temperature under (a) Li-rich, (b) Li&Mn-mid, and (c) Mn-rich conditions. The enriched elements in the non-STO surfaces are denoted following their surface indices.

investigated and compared below. The surface influence zones (SIZs) of these terminals are considered with a thickness (d) of 3 or 5 Å, based on the results of Section S6† and considering the computing resources. The schematic diagram of the surface influence zone is shown in Fig. 6(a). It should be noted that with the extraction of Li ions on the Li_2MnO_3 surface, O ions form oxygen on the system surface and surface reconstruction occurs according to earlier research.[6,9,14,27] Therefore, the scope of this study is mainly limited to the period prior to the initial stage of oxygen release. In this section, we focus on the conductivity characteristics and theoretical average charge voltage of the different surfaces and terminals, as well as the oxygen evolution properties on the different surfaces and terminals. Finally, the oxygen evolution characteristics of each terminal are scored and compared. The detailed research and calculation results are shown in Fig. 6(b–f). Of note, the black dashed lines in Fig. 6(b) and (c) represent the calculated values for the band gap and the average platform of the bulk structure, respectively, which are in agreement with the results of the experiments.[6,55]

Firstly, the electrochemical characteristics of different surfaces and terminals of Li_2MnO_3 are discussed as follows. From Fig. 6(b), in addition to the (110) surface exhibiting conductor properties, the band gap values of the (111), (11$\bar{1}$), (10$\bar{1}$), (010), and (131) surfaces are also smaller than those of the bulk structure (the corresponding density of states for different surfaces and terminals of Li_2MnO_3, as well as the bulk structure, can be found in Fig. S16†). Meanwhile, the terminal of (111)_Li1 has the lowest discharge platform (*cf.* Section S7†) as shown in Fig. 6(c), indicating that this surface is the first to extract Li ions during the charging process. Except for the (001) surface, the discharge voltages of all other surfaces are lower than that of the bulk structure. Combining Fig. 6(b) and (c), the band gap value and voltage platform of the (001)_STO terminal are 1.73 eV and 4.67 V, respectively, which are higher than the 1.65 eV and 4.5 V of the bulk Li_2MnO_3 structure. This indicates that (001)_STO has poor conductivity and acts as an inert surface during the charging process.

Secondly, the oxygen evolution properties (as seen in Section S8†) at the different surfaces and terminals are discussed below. The terminal of (010)_Mn0.5O0.5 has the lowest Li-ion residual rate of only 20% (*cf.* Fig. 6(d)), indicating that it has good oxygen evolution prevention properties. In comparison, the (110)_Li1.5O1 and (010)_Li1O1 terminals exhibit the worst lithium ion residual rate of up to 83.3%, indicating that they have poor oxygen evolution inhibition properties. Overall, Mn&O-rich terminals can effectively inhibit the evolution of oxygen, followed by Li-rich and STO terminals, while Li&O-rich terminals exhibit the worst oxygen inhibition properties. In addition, Fig. 6(e) shows that the surfaces of (10$\bar{1}$), (001), and (131), which satisfy the stoichiometric relationship, have a low number of released oxygen molecules per unit area, while the surfaces of (010), (110), and (11$\bar{1}$) exhibit the opposite situation, and the surface of (111) is intermediate between the others.

Finally, to facilitate the description of the oxygen release properties of each terminal, we attempt to evaluate the oxygen activity of each surface based on the residual oxygen ion concentration and the number of oxygen molecules released per unit area by each terminal. The scoring criteria are as follows:

$$SSP = \left[\frac{1}{2}\left(\frac{O_{vc}^{min}}{O_{vc}{}^{i}}\right) + \frac{1}{2}\left(\frac{Li_{vc}{}^{i}}{Li_{vc}^{max}}\right)\right] \times 100 \quad (15)$$

Here, SSP stands for the score of oxygen release properties of different terminals. O_{vc}^{min} is the minimum value for all different surfaces and terminals at the initial stage of oxygen release per unit area. Li_{vc}^{max} is the maximum concentration of Li vacancies for all different surfaces and terminals with the initial oxygen release. $O_{vc}{}^{i}$ and $Li_{vc}{}^{i}$ are the values of oxygen release per unit area and the concentration of Li vacancies in surface i, respectively, at the initial stage of oxygen release. The values of SSP are

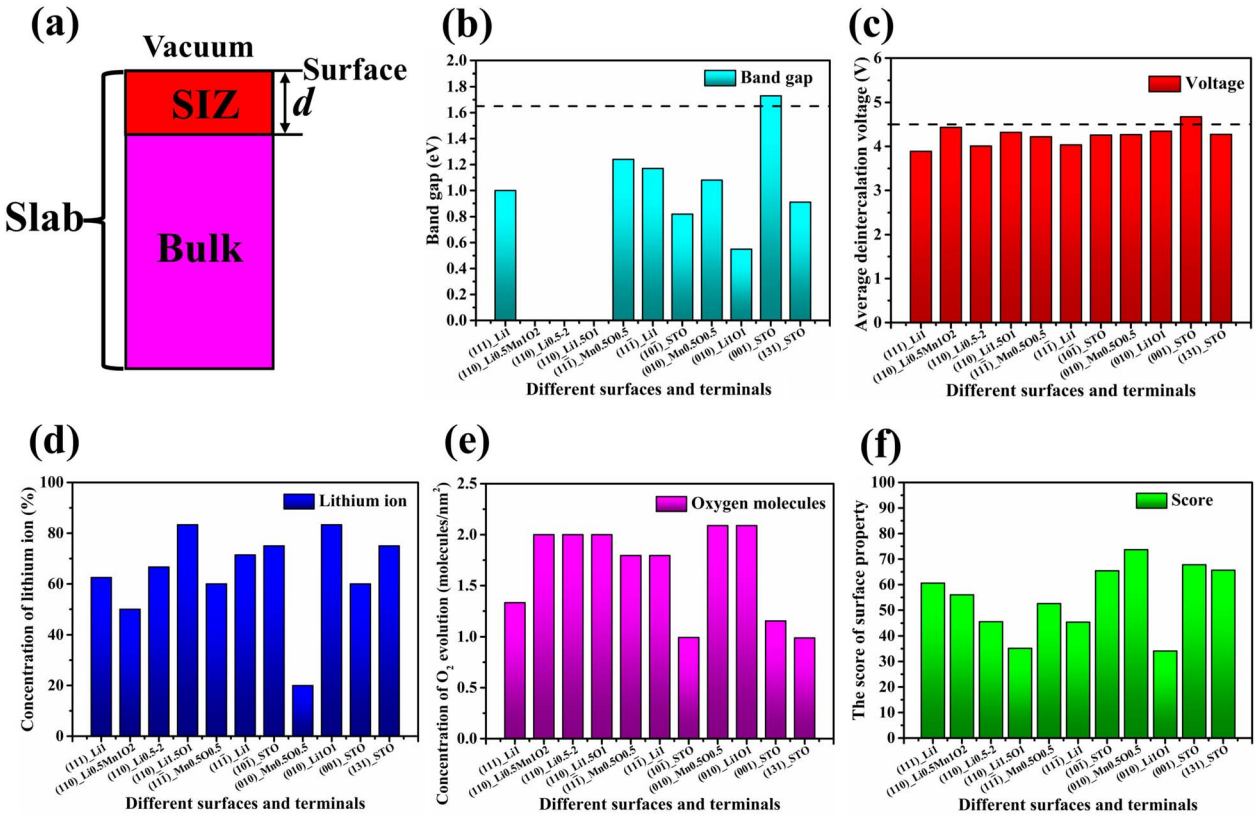

Fig. 6 (a) The schematic diagram of surface influence zone (SIZ). (b) The band gaps of different surfaces and terminals. (c) The theoretical average charging voltages of different surfaces and terminals in the SIZ. (d) The Li-ion concentrations at the initial stage of the oxygen release in the SIZ for different surfaces and terminals. (e) The numbers of oxygen molecules per unit area at initial stage of the oxygen release from different surfaces and terminals. (f) The scores of oxygen evolution inhibition at different surfaces and terminals.

shown in Fig. 6(f). It shows that the terminal of (010)_Mn0.5O0.5 has the best surface oxygen suppression performance, followed by terminals $(10\bar{1})$, (001), and (131), which meet stoichiometric ratios. However, the terminals of (110)_Li1.5O1 and (010)_Li1O1 exhibit the worst oxygen suppression characteristics.

In order to explain the difference in the oxygen release suppression effect for the various terminals, the density of states (DOS, *cf.* Fig. 7) of O ions at different terminals and the p-band center (E_p) are investigated. The formula of E_p is expressed as below (here $\rho_p(E)$ repersents the density of states):

$$E_p = \frac{\int_{-\infty}^{+\infty} E\rho_p(E)\mathrm{d}E}{\int_{-\infty}^{+\infty} \rho_p(E)\mathrm{d}E} \quad (16)$$

The Mn&O-rich terminals are advantageous for inhibiting oxygen evolution. As shown in Fig. 7(a), they have a low p-band center of the O ions, indicating that the electrons of the O ions occupy a low electronic energy level. Therefore, during the charging process, it is more difficult to oxidize the -2 charges of the O ions to $-m$ ($m < 2$) valence O ions. This effectively inhibits the evolution of oxygen. However, for Li&O-rich terminals, the inhibition of oxygen release is poor. The p-band centers of the O ions have high values (as seen in Fig. 7(b)), indicating that the electrons of the O ions occupy higher energy levels in these systems. This allows them to lose electrons more easily during the lithium removal process. Similarly, the ability of the other terminals to suppress oxygen evolution is consistent with the position of their O ions' p-band center.

The different terminals have different p-band centers of O ions. This is mainly due to the coordination number of Mn ions around the surface O ions. According to Fig. S16,† the electrons of Mn ions mainly occupy lower energy levels with respect to those of O ions. Similarly, the electrons provided by Mn ions to O^{2-} ions also occupy low energy levels, so the p-band center of the O ions is reduced with more Mn–O bonds. For example, in Mn&O-rich terminals, the O ions have low p-band centers due to their high Mn-ion coordination numbers. However, in Li&O-rich terminals, there are the high p-band centers for their O ions due to the small number of Mn ions surrounding the O ions. Furthermore, according to the Mn–O bond strength from Section S3† and the integrated crystal orbital Hamilton population (ICOHP)[56,57] of Mn–O in Section S6,† we find that the Mn–O bond has a higher bond strength compared to the Li–O bond. This is beneficial for preventing the evolution of oxygen.

The Hirshfeld-I charge[58–60] differences (relative to the bulk structure) of the initially released O ions and their surrounding Mn ions, at different Li-ion concentrations and for the different surfaces and terminals, are also shown in Fig. 7. Here,

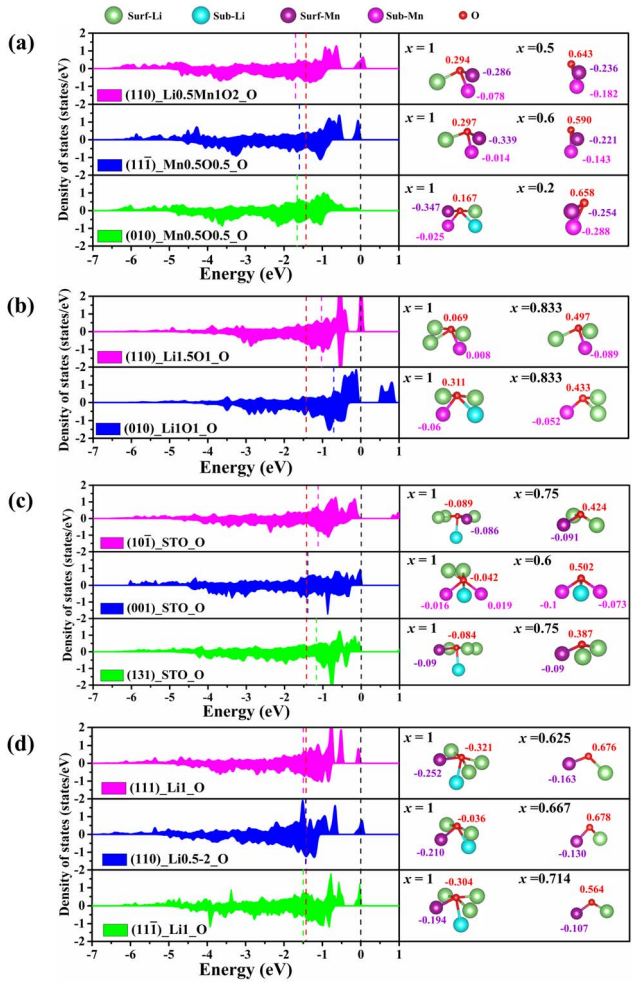

Fig. 7 The density of states of O ions for different terminals (a)–(d) as shown in the plots, as well as the Hirshfeld-I charge difference of the initially released O ions and their surrounding Mn ions relative to the bulk structure at different Li-ion concentrations. (The black and red dotted lines represent the Fermi energy level and the bulk structure of the O ion p-band center, respectively, and the other colored dotted lines represent the p-band centers of different terminal O ions. The *x* values in the right column are the concentrations of Li ions for the complete structure and the initial stage of oxygen release, respectively.)

a negative value indicates electron accumulation, while a positive value indicates electron depletion. Note that the average Hirshfeld-I charge values of Li, Mn, and O are +1.029, +1.836, and −1.298, respectively, under the bulk structure conditions. This implies that electrons dissipate from the surfaces of the O ions when Li ions are extracted. However, for the Mn ions, during the process of Li-ion removal, except for the surface Mn ions, which exhibit a slight electron loss, almost all of the subsurface Mn ions gain electrons instead. This situation indicates that the charge compensation at the surfaces of the system during the charging process is mainly by O ions and the participation of Mn ions is very limited.[61]

Moreover, compared with the Hirshfeld-I charges of O ions in the bulk structure, the initially released O ions exhibit charge loss at the Mn&O-rich terminals and the Li&O-rich terminals,

Table 2 The values of n_{Li}, n_{Mn}, H_S, H_B, and ΔC (in *e*)

Terminal	n_{Li}	n_{Mn}	H_S	H_B	ΔC
(110)_Li0.5Mn1O2	1	2	−1.004	−0.783	−0.221
(11$\bar{1}$)_Mn0.5O0.5	1	2	−1.001	−0.783	−0.218
(010)_Mn0.5O0.5	2	2	−1.131	−0.955	−0.176
(110)_Li1.5O1	3	1	−1.229	−0.820	−0.409
(010)_Li1O1	3	1	−0.987	−0.820	−0.167
(10$\bar{1}$)_STO	4	1	−1.387	−0.992	−0.395
(001)_STO	3	2	−1.340	−1.126	−0.214
(131)_STO	4	1	−1.382	−0.992	−0.390
(111)_Li1	4	1	−1.619	−0.992	−0.627
(110)_Li0.5–2	3	1	−1.334	−0.820	−0.514
(11$\bar{1}$)_Li1	4	1	−1.602	−0.992	−0.610

while the STO terminals and the Li-rich terminals gain electrons. To clarify this issue, the values of the Hirshfeld-I charges of the initially released O ions (H_S) are listed in Table 2. Meanwhile, the coordination numbers of the Li ions (n_{Li}) and Mn ions (n_{Mn}) around them are also listed. Additionally, Table 2 shows the number of Hirshfeld-I charges (H_B) obtained by the O ion in the bulk structure under these coordination conditions, as well as the difference ΔC between H_S and H_B. From Fig. 7 and Table 2, it is clear that the electron loss is mainly due to the fact that the O ions are not fully coordinated at the surface. Therefore, the number of electrons obtained is less than that in the bulk structure. However, the gain of electrons is mainly due to the fact that the Li or Mn ions on the surface have not reached a fully coordinated state (as seen in Section S9†). Their large number of unpaired electrons are redistributed around the O ions. In summary, the number of coordinated O ions on the surface and the redistribution of unpaired electrons are different for any surface. Therefore, the O ions at different terminals have different Hirshfeld-I charge numbers.

3.4 Explanation of the grain morphology of Li_2MnO_3

Experimental studies have shown that Li_2MnO_3 exhibits a dish-shape grain morphology, growing preferentially along the (001) surface.[17,26] In general, the grains grow preferentially along the surface that has a low surface energy, which has the advantage of mitigating the total energy increase caused by the increase in system surface area. When the grains grow perpendicular to the surface, different terminals of the surface occur cyclically during the growth process. Therefore, the smaller difference in terminal energies is advantageous for rapid growth perpendicular to the surface direction. From Section S10,† it is clear that the different terminals of the (001) surface have a very high energy difference (the minimum value is 3.867 J m^{-2}) throughout the synthesis temperature range at the different chemical potentials. However, for other common surfaces of Li_2MnO_3 grains, the energy difference is low (the maximum value is 2.247 J m^{-2}), which enables rapid grain growth. Accordingly, the surface energy of the (001)_STO terminal of Li_2MnO_3 is only 0.995 J m^{-2} (the minimum surface energy of common surfaces is 0.873 J m^{-2}). This low surface energy does not increase the total surface energy with the increase in the surface area of the system. Based

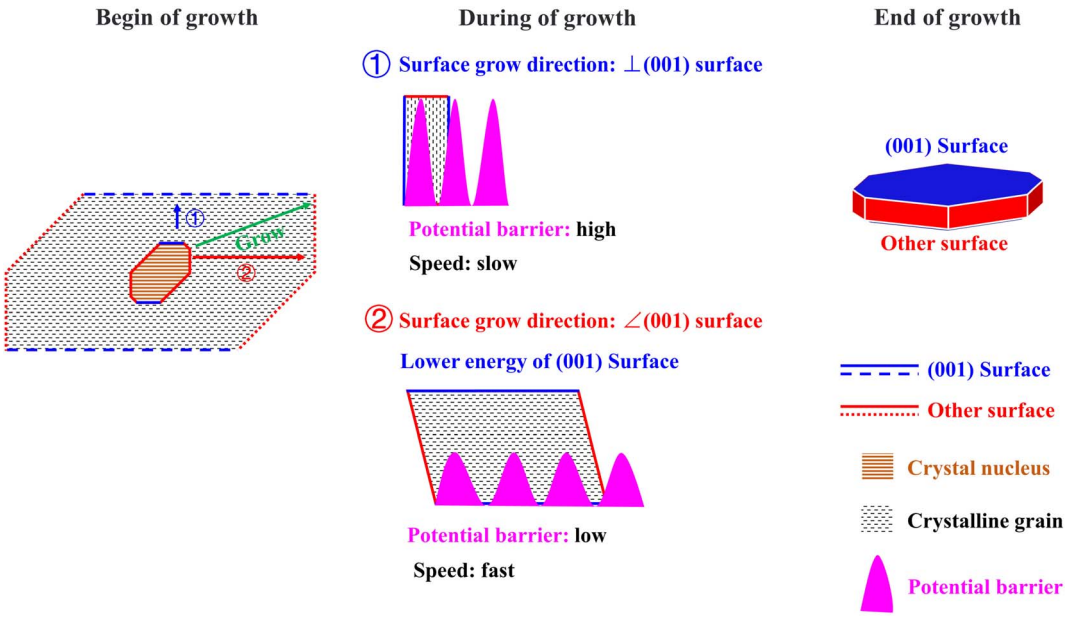

Fig. 8 The sketched growth process of the Li_2MnO_3 grain morphology.

on the above analysis, the growth process of the Li_2MnO_3 grain morphology is shown in Fig. 8.

As shown in Fig. 8, Li_2MnO_3 starts to nucleate at the beginning of the reaction according to the Wulff theory. At this time, the surface energy of the (001) surface is not sufficient to make it the dominant surface. In the subsequent grain growth process, it is difficult for Li_2MnO_3 to grow rapidly along the [001] direction because of the high barrier. However, when other surfaces with an angle to the (001) surface form, the grains grow rapidly in the direction perpendicular to these surfaces due to the low energy barrier. At the same time, the (001)_STO terminal, with its large surface area, is also stable due to its low surface energy. Thus, when the reaction is completed, the grain morphology takes the form of a dish-shape.

4 Conclusions

In summary, we have systematically investigated the surface stability, the electrochemical properties of the stable surfaces, the oxygen evolution properties of the stable surfaces, and grain morphology of Li_2MnO_3 *via* first-principles calculations. It is demonstrated that the defect-containing (001) surface of Li_2MnO_3 satisfies the stoichiometric relationship in terms of surface stability under air and in the main experimental temperature range of the synthesis. The terminals satisfying the stoichiometric ratio, (001)_STO, (131)_STO, and (10$\bar{1}$)_STO, exhibit low surface energies. With increasing temperature, the area percentage of surfaces satisfying the stoichiometric ratio (STO terminals) decreases, while the area percentage of the dominant (11$\bar{1}$) surface increases. The crystal surface changes from a Li-rich shell to a Mn-rich shell as the Mn content increases. In terms of electrochemical properties, all the other surfaces exhibit good electrochemical properties, except for the poor charge voltage and conductivity of the (001)_STO terminal compared to the bulk structure. The differences in the inhibition performance of oxygen release during the Li-ion removal process for the different surfaces are mainly due to the position of the O ion p-band center and the stronger Mn–O bond strength. The (010)_Mn0.5O0.5, (001)_STO, (10$\bar{1}$)_STO, and (131)_STO terminals show a better inhibition of oxygen release under the adopted evaluation criteria. In addition, the low surface energy of the (001) surface and its high energy barrier between the different terminals are critical to the dish-shape appearance of the grain morphology. This understanding of the surface evolution may further promote Li_2MnO_3 as a cathode material for high-energy-density Li-ion batteries.

Author contributions

Xiaotong Yan: methodology, investigation, formal analysis, visualization, writing – original draft. Xingyu Zhou: methodology, writing – review & editing. Chunwei Zhu: methodology, writing – review & editing. Weijie Huang: methodology, writing – review & editing. Yu-Jun Zhao: conceptualization, supervision, resources, writing – review & editing, funding acquisition.

Conflicts of interest

There are no conflicts to declare.

Acknowledgements

This work is financially supported by National Natural Science Foundation of China (Grant No. 12074126), and the Foundation for Innovative Research Groups of the National Natural Science Foundation of China (Grant No. 51621001).

References

1 D. Larcher and J.-M. Tarascon, *Nat. Chem.*, 2015, **7**, 19–29.
2 M. Shahjalal, P. K. Roy, T. Shams, A. Fly, J. I. Chowdhury, M. R. Ahmed and K. Liu, *Energy*, 2022, **241**, 122881.
3 Y. Yang, E. G. Okonkwo, G. Huang, S. Xu, W. Sun and Y. He, *Energy Storage Mater.*, 2021, **36**, 186–212.
4 Z. Zhu, T. Jiang, M. Ali, Y. Meng, Y. Jin, Y. Cui and W. Chen, *Chem. Rev.*, 2022, **122**, 16610–16751.
5 J. Neumann, M. Petranikova, M. Meeus, J. D. Gamarra, R. Younesi, M. Winter and S. Nowak, *Adv. Energy Mater.*, 2022, **12**, 2102917.
6 N. Guerrini, L. Jin, J. G. Lozano, K. Luo, A. Sobkowiak, K. Tsuruta, F. Massel, L.-C. Duda, M. R. Roberts and P. G. Bruce, *Chem. Mater.*, 2020, **32**, 3733–3740.
7 E. Cho, K. Kim, C. Jung, S.-W. Seo, K. Min, H. S. Lee, G.-S. Park and J. Shin, *J. Phys. Chem. C*, 2017, **121**, 21118–21127.
8 P. K. Nayak, E. M. Erickson, F. Schipper, T. R. Penki, N. Munichandraiah, P. Adelhelm, H. Sclar, F. Amalraj, B. Markovsky and D. Aurbach, *Adv. Energy Mater.*, 2018, **8**, 1702397.
9 P. Yan, L. Xiao, J. Zheng, Y. Zhou, Y. He, X. Zu, S. X. Mao, J. Xiao, F. Gao, J.-G. Zhang and C.-M. Wang, *Chem. Mater.*, 2015, **27**, 975–982.
10 D. Eum, B. Kim, S. J. Kim, H. Park, J. Wu, S.-P. Cho, G. Yoon, M. H. Lee, S.-K. Jung, W. Yang, W. M. Seong, K. Ku, O. Tamwattana, S. K. Park, I. Hwang and K. Kang, *Nat. Mater.*, 2020, **19**, 419–427.
11 Z. Zhuo, K. Dai, R. Qiao, R. Wang, J. Wu, Y. Liu, J. Peng, L. Chen, Y.-d. Chuang, F. Pan, Z.-x. Shen, G. Liu, H. Li, T. P. Devereaux and W. Yang, *Joule*, 2021, **5**, 975–997.
12 R. A. House, J.-J. Marie, M. A. Pérez-Osorio, G. J. Rees, E. Boivin and P. G. Bruce, *Nat. Energy*, 2021, **6**, 781–789.
13 H. Chen and M. S. Islam, *Chem. Mater.*, 2016, **28**, 6656–6663.
14 J. Rana, J. K. Papp, Z. Lebens-Higgins, M. Zuba, L. A. Kaufman, A. Goel, R. Schmuch, M. Winter, M. S. Whittingham, W. Yang, B. D. McCloskey and L. F. J. Piper, *ACS Energy Lett.*, 2020, **5**, 634–641.
15 Z. Yin, H. Zhu, Y. Huang, D. Luo, Y. Ren, S. Lan and Q. Liu, *J. Mater. Chem. A*, 2022, **10**, 19387–19411.
16 Q. He, B. Yu, Z. Li and Y. Zhao, *Energy Environ. Mater.*, 2019, **2**, 264–279.
17 A. Quesne-Turin, D. Flahaut, L. Croguennec, G. Vallverdu, J. Allouche, Y. Charles-Blin, J.-N. Chotard, M. Ménétrier and I. Baraille, *ACS Appl. Mater. Interfaces*, 2017, **9**, 44222–44230.
18 J.-M. Lim, D. Kim, Y.-G. Lim, M.-S. Park, Y.-J. Kim, M. Cho and K. Cho, *J. Mater. Chem. A*, 2015, **3**, 7066–7076.
19 Y. Xie, M. Saubanère and M.-L. Doublet, *Energy Environ. Sci.*, 2017, **10**, 266–274.
20 D. Kramer and G. Ceder, *Chem. Mater.*, 2009, **21**, 3799–3809.
21 B. Qiu, M. Zhang, L. Wu, J. Wang, Y. Xia, D. Qian, H. Liu, S. Hy, Y. Chen, K. An, Y. Zhu, Z. Liu and Y. S. Meng, *Nat. Commun.*, 2016, **7**, 12108.
22 F. Ning, H. Shang, B. Li, N. Jiang, R. Zou and D. Xia, *Energy Storage Mater.*, 2019, **22**, 113–119.
23 Y. Shin, W. H. Kan, M. Aykol, J. K. Papp, B. D. McCloskey, G. Chen and K. A. Persson, *Nat. Commun.*, 2018, **9**, 4597.
24 Y. Shin and K. A. Persson, *ACS Appl. Mater. Interfaces*, 2016, **8**, 25595–25602.
25 L. Wang, S. Zhao, B. Wang and H. Yu, *J. Energy Chem.*, 2023, **81**, 110–117.
26 A. Boulineau, L. Croguennec, C. Delmas and F. Weill, *Solid State Ionics*, 2010, **180**, 1652–1659.
27 D. Kim, J.-M. Lim, Y.-G. Lim, M.-S. Park, Y.-J. Kim, M. Cho and K. Cho, *ChemSusChem*, 2015, **8**, 3255–3262.
28 X. Yang, W. Tang, H. Kanoh and K. Ooi, *J. Mater. Chem.*, 1999, **9**, 2683–2690.
29 G. Kresse and D. Joubert, *Phys. Rev. B: Condens. Matter Mater. Phys.*, 1999, **59**, 1758–1775.
30 G. Kresse and J. Furthmüller, *Comput. Mater. Sci.*, 1996, **6**, 15–50.
31 G. Kresse and J. Furthmüller, *Phys. Rev. B: Condens. Matter Mater. Phys.*, 1996, **54**, 11169.
32 J. P. Perdew, K. Burke and M. Ernzerhof, *Phys. Rev. Lett.*, 1996, **77**, 3865.
33 V. I. Anisimov, J. Zaanen and O. K. Andersen, *Phys. Rev. B: Condens. Matter Mater. Phys.*, 1991, **44**, 943–954.
34 F. Zhou, M. Cococcioni, C. A. Marianetti, D. Morgan and G. Ceder, *Phys. Rev. B: Condens. Matter Mater. Phys.*, 2004, **70**, 235121.
35 A. Togo, L. Chaput, T. Tadano and I. Tanaka, *J. Phys.: Condens. Matter*, 2023, **35**, 353001.
36 A. Togo, *J. Phys. Soc. Jpn.*, 2023, **92**, 012001.
37 P. Canepa, J. A. Dawson, G. Sai Gautam, J. M. Statham, S. C. Parker and M. S. Islam, *Chem. Mater.*, 2018, **30**, 3019–3027.
38 B. Gao, R. Jalem and Y. Tateyama, *ACS Appl. Mater. Interfaces*, 2020, **12**, 16350–16358.
39 K. Reuter and M. Scheffler, *Phys. Rev. B: Condens. Matter Mater. Phys.*, 2001, **65**, 035406.
40 M. W. Chase, NIST-JANAF Thermochemical Tables, American Institute of Physics, 1998, 4th edn, p. 1728.
41 S. P. Ong, W. D. Richards, A. Jain, G. Hautier, M. Kocher, S. Cholia, D. Gunter, V. L. Chevrier, K. A. Persson and G. Ceder, *Comput. Mater. Sci.*, 2013, **68**, 314–319.
42 A. Boulineau, L. Croguennec, C. Delmas and F. Weill, *Chem. Mater.*, 2009, **21**, 4216–4222.
43 S.-Q. Yang, C.-B. Li, J. Du and Y.-J. Zhao, *Appl. Surf. Sci.*, 2019, **491**, 187–194.
44 K. Hoang and M. D. Johannes, *J. Mater. Chem. A*, 2014, **2**, 5224–5235.
45 L. Wang, F. Zhou, Y. S. Meng and G. Ceder, *Phys. Rev. B: Condens. Matter Mater. Phys.*, 2007, **76**, 165435.
46 M. Fishman, H. L. Zhuang, K. Mathew, W. Dirschka and R. G. Hennig, *Phys. Rev. B: Condens. Matter Mater. Phys.*, 2013, **87**, 245402.
47 M. Xu, J. Yang, J. Zheng and F. Pan, *Comput. Mater. Sci.*, 2017, **137**, 113–118.
48 J. Jiao, G. Lai, S. Qin, C. Fang, X. Xu, Y. Jiang, C. Ouyang and J. Zheng, *Acta Mater.*, 2022, **238**, 118229.

49 S. Wang, E. Tian and C. Lung, *J. Phys. Chem. Solids*, 2000, **61**, 1295–1300.
50 M. Yan, S. Chen, T. Mitchell, D. Gay, S. Vyas and R. Grimes, *Philos. Mag. A*, 1995, **72**, 121–138.
51 W.-B. Zhang, C. Chen and S.-Y. Zhang, *J. Phys. Chem. C*, 2013, **117**, 21274–21280.
52 I. Galanakis, G. Bihlmayer, V. Bellini, N. Papanikolaou, R. Zeller, S. Blügel and P. H. Dederichs, *Europhys. Lett.*, 2002, **58**, 751–757.
53 G. Wulff, *Z. Kristallogr.*, 1901, **34**, 449.
54 C. Boukouvala, J. Daniel and E. Ringe, *Nano Convergence*, 2021, **8**, 26.
55 M. Ranjeh, M. Masjedi-Arani, M. Salavati-Niasari and H. Moayedi, *J. Mol. Liq.*, 2020, **300**, 112292.
56 V. L. Deringer, A. L. Tchougréeff and R. Dronskowski, *J. Phys. Chem. A*, 2011, **115**, 5461–5466.
57 R. Nelson, C. Ertural, J. George, V. L. Deringer, G. Hautier and R. Dronskowski, *J. Comput. Chem.*, 2020, **41**, 1931–1940.
58 F. L. Hirshfeld, *Theor. Chim. Acta*, 1977, **44**, 129–138.
59 P. Bultinck, C. Van Alsenoy, P. W. Ayers and R. Carbó-Dorca, *J. Chem. Phys.*, 2007, **126**, 144111.
60 K. Finzel, Á. M. Pendás and E. Francisco, *J. Chem. Phys.*, 2015, **143**, 084115.
61 M. Oishi, K. Yamanaka, I. Watanabe, K. Shimoda, T. Matsunaga, H. Arai, Y. Ukyo, Y. Uchimoto, Z. Ogumi and T. Ohta, *J. Mater. Chem. A*, 2016, **4**, 9293–9302.